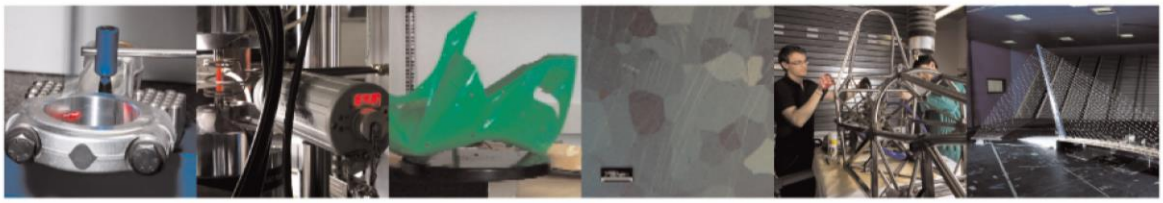

Comparative Study of Pure Iron Manufactured by Selective Laser Melting, Laser Metal Deposition, and Casting Processes

Carluccio, Danilo; Bermingham, Michael; Kent, Damon; Demir, Ali Gökhan; Previtali, Barbara; Dargusch, Matthew S.

Comparative Study of Pure Iron Manufactured by Selective Laser Melting, Laser Metal Deposition, and Casting Processes

D. Carluccio[ac1], M. Bermingham[ac], D. Kent[acd], A.G. Demir[b], B. Previtali[b], M.S. Dargusch[ac]

[a] School of Mechanical and Mining Engineering and Queensland Centre for Advanced Materials Processing and Manufacturing (AMPAM), The University of Queensland, Australia

[b] Department of Mechanical Engineering, Politecnico di Milano, Via La Masa 1, 20156 Milan, Italy

[c] Australian Research Council Research Hub for Advanced Manufacturing of Medical Devices

[d] School of Science and Engineering, University of the Sunshine Coast, Maroochydore DC, QLD 4558, Australia

Abstract

Laser based additive manufacturing (AM) processes such as laser metal deposition (LMD) and selective laser melting (SLM) can produce patient-specific implants with minimal post-processing and shorter lead times compared to conventional manufacturing methods. In this study the microstructural, mechanical and corrosion properties of cast, LMD and SLM manufactured pure Fe for biodegradable biomedical implants were compared. It was found that casting resulted in an average grain size double that of pure Fe manufactured via LMD and over 30 times that when compared to parts manufactured using SLM. This was attributed to the higher cooling rates of the laser-based AM technologies and led to superior mechanical properties of the samples manufactured via SLM. The corrosion rate of the LMD and SLM samples were approximately fifty percent higher than the cast pure Fe. For biodegradable Fe implants a higher corrosion rate and yield stress are preferential, and combined with the ability to produce complex geometries, makes SLM a promising manufacturing technology for biodegradable implants such as bone scaffolds.

Keywords

Biodegradable Iron; Corrosion; Mechanical Properties; Microstructure; Additive Manufacturing

[1] Corresponding author: d.carluccio@uq.edu.au

Introduction

Biodegradable metals (BDM) have garnered significant interest recently as a replacement for permanent metals used for medical devices such as fixtures, bone scaffolds, stents and sutures [1]. Many of these medical devices are implanted to support temporary problems, and following full healing, the devices are either removed or left in the body. The former requires a second surgery to remove the implant, decreasing the patient comfort and increasing the chance of surgical complications. The latter can result in the body mounting an innate immune response to foreign bodies that cannot be phagocytosed possibly causing implant loosening [2]. Furthermore, implants left in the body also have a higher chance of toxic ions leaching out over time causing in peri-implant cell death [3]. BDM implants provide similar functions to permanent metal implants but subsequent to full healing slowly degrade away. An ideal BDM should retain adequate mechanical properties to allow for tissue healing and slowly transfer the stress back to the healed tissue as the implant degrades [1]. The implant material should invoke an adequate host response to both the initial implantation and the following degradation. Therefore, the major degradation constituent should be an essential element the body can metabolise successfully in large doses [4]. The most researched BDMs so far have been magnesium, zinc and iron [1, 4].

Magnesium has been extensively researched as a biodegradable implant material with clinicians trialling pure Mg as early as the 19th century [1, 5]. It is an essential macronutrient that is processed very efficiently by the human body in large quantities [6]. However, Mg can be difficult to manufacture into implants because of its relatively poor formability [7]. Furthermore, the mechanical integrity of Mg implants is often compromised during healing because of its high corrosion rate [1, 5]. The corrosion of Mg also results in the release of hydrogen gas bubbles, which can severely affect the surrounding tissue healing, especially in bone implants [8]. Zn has recently gathered a lot of interest because of its favourable corrosion rate for biodegradable implant applications [9]. However, Zn is mostly used as an alloying element and rarely the main constituent because of its poor mechanical properties [10]. Furthermore, there has been insufficient research on the toxicity of Zn *in vivo* as a biodegradable implant [11]. Fe can also be toxic in high doses, however, Fe toxicity cases are rare because iron levels are regulated through absorption rather than secretion, as is the case with Zn [12]. The primary concern with Fe as a biodegradable metal is its slow corrosion rate [13] that can invoke similar foreign body reactions to permanent implants [14]. On top of this α-Fe is ferromagnetic which can reduce MRI compatibility [15]. However, compared to Mg and Zn, Fe has excellent mechanical properties, similar to that of 316L stainless steel [15] and

unlike Mg its degradation does not result in hydrogen evolution. Furthermore, it is relatively inexpensive and easy to manufacture [16]. Fe has been used as an implant material for centuries mostly due to its processability, however, it was only in the last century that Fe has been more extensively researched specifically for biodegradable implant applications [1].

Conventional manufacturing methods such as casting often require further post processing to achieve the final product [17]. On the other hand, laser based additive manufacturing (AM) processes such as laser metal deposition (LMD) and selective laser melting (SLM) can produce implants with minimal post-processing and shorter lead times. Compared to LMD, SLM is able to produce more complex geometries with hierarchal porosities, which lends itself to applications such as bone scaffolds [18, 19]. Research on the SLM of pure Fe for biomedical applications has been relatively limited, with the majority of research concentrated on steels commonly used in industry [20]. High density bulk pure Fe [21-23] and high quality pure Fe porous scaffolds [19] have been successfully manufactured using SLM. However, these studies mostly focused on processing and comparisons to traditionally manufactured pure iron. Similarly, to date, comparison studies have mostly focused on comparing novel manufacturing methods or alloys to conventionally manufactured pure iron [24-26]. It can be ambiguous to directly compare the corrosion results of different studies as it is significantly influenced by experimental parameters [27]. Therefore it is important to directly compare the effect of net-shape manufacturing techniques on the properties of pure Fe for biomedical applications. The paper is the first to compare the microstructural, mechanical and corrosion properties of cast, LMD and SLM manufactured pure Fe for biomedical applications.

2.0 Materials and Method

2.1 Materials

Cast samples were prepared from a high purity iron ingot (composition shown in Table 1) melted in an induction furnace (Powertrak 20-96R, Inductotherm, USA) in an alumina crucible coated with zirconium silicate. Prior to pouring a steel mould was pre-coated with boron nitride and preheated to 300 C. The melt was poured into the mould and cooled in air. Samples were machined from the centre of the casting for subsequent testing.

Table 1 Inductively coupled plasma atomic emission spectroscopyanalysis showing the composition of samples in wt%

Sample	Fe %	C %	Mn %	Si %	S %	P %	Ni %	Cr %	Mo (%)
Cast	Bal.	0.01	0.01	< 0.02	0.01	< 0.01	< 0.01	0.01	< 0.01
LMD	Bal.	0.01	0.09	< 0.02	0.01	0.01	0.02	0.03	0.02
SLM	Bal.	0.01	0.01	< 0.02	0.01	0.01	< 0.01	0.03	0.01

Laser metal deposition (LMD) samples were manufactured in a LENS® 450 system (Optomec, Albuquerque, USA) using 99.8% purity Fe powder, shown in Figure 1, with particle size distribution between 45-106 µm (Wako, Osaka, Japan). Cylindrical parts were manufactured using a 400 W Nd:YAG continuous laser with laser power (P) of 375 W, scan speed (v) of 8.5 mm/s, layer thickness (z) of 0.510 mm and hatch distance (d_h) of 0.762 mm. LMD was performed under argon with oxygen levels below 10 ppm to minimise oxidation. Afterwards parts were machined to the required sample dimensions.

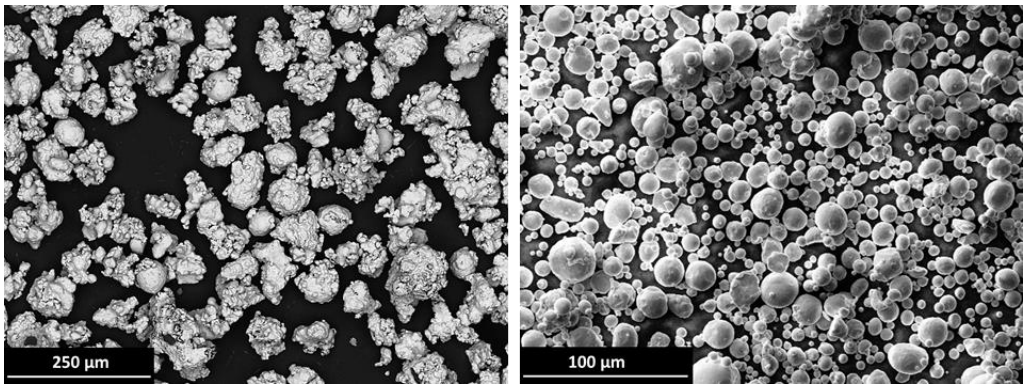

Figure 1 Scanning electron microscope image showing the powder morphologies of the iron powder for LMD (left) and SLM (right)

Selective laser melted (SLM) samples were manufactured on a commercial SLM system (Renishaw, AM250, Stone, UK) using spherical Fe powder with a purity of 99.8 % (Table 1) and particle size distribution ≤45 µm (TLS Technik, Bitterfield, Germany). The machine is equipped with a 200 W single mode fibre laser using pulsed wave emission. The reduced build platform (RBV) system was employed reducing the build volume of the machine to 78x78x50 mm^3. Mild steel base plates were used for producing the specimens. Cylindrical Fe samples were manufactured under an argon atmosphere with oxygen content maintained below 1000 ppm using a power (P) of 200 W, a pulse

duration (t_{on}) of 100 µs, point distance (d_p) of 60 µm, hatch spacing (d_h) of 100 µm and layer thickness (z) of 50 µm. Focal position was kept at the powder bed surface, producing a beam diameter of 70 µm. The energy density of the two laser based AM processes were compared. For LMD it is defined as:

$$E = \frac{P}{v d_h z} \quad (1)$$

And for SLM:

$$E = \frac{P t_{on}}{d_p d_h z} \quad (2)$$

The density was measured using Archimedes' principle with a procedure based on ISO 3369 [28]. . Three samples were measured independently at least 3 times in air and in H-Galden (ZT180, Solvay, Japan). High density components were achieved as shown in Table 2. Samples were analysed as-built conditions without any heat treatment to reveal the effect of the manufacturing process.

Table 2 Density and percentage density of each manufacturing method

	ρ (g/cm^3)	% Density
Cast	7.87 ± 1.8E^{-3}	99.9 ± 0.02
LMD	7.84 ± 4.4E^{-3}	99.6 ± 0.06
SLM	7.81 ± 2.2E^{-3}	99.2 ± 0.03

2.2 Material Characterization

Additive manufactured samples were cut in the plane perpendicular (build direction out of plane) and parallel (build direction in plane) to the scan direction. All samples were mounted, ground and mechanically polished following standard metallographic procedures. Samples were etched with Nital Solution to reveal the microstructure. Optical microscopy (Polyvar Met, Reichert, USA) was used to observe the microstructure. Grain size analysis was performed using the linear intercept method based on ASTM E112-13 [29].

XRD measurements were performed on a BrukerD8 (Bruker, Billerica, USA) with Cu Kα radiation with a voltage of 40kV and current of 40mA.

2.3 Mechanical Characterization

Compression testing was performed according to ASTM E9 - 09 [30]. ASTM F3122 - 14 states that the procedures mentioned in ASTM E9 - 09 are suitable for additive manufactured solid cylindrical samples [31]. As such, AM samples were compressed in the build direction, and all samples were tested under the same conditions. A minimum of three compression specimen per manufacturing method were machined to have a height-to-diameter ratio of 1.75. Uniaxial compression tests (Shimadzu AGS-100kNX, Kyoto, Japan) were performed on flat, hard, parallel plates with a crosshead speed of 2 mm/min at room temperature.

2.4 Electrochemical Test

Potentiodynamic polarisation tests based on ASTM G59-97 [32] were performed to compare the electrochemical corrosion performance of the samples. Additively manufactured samples were cross-sectioned perpendicular to the build direction. Specimens with an exposed surface area of approximately 1.77 cm^2 were connected to a copper wire and cold mounted in epoxy. The mounted samples were mechanically polished to 1200 grit, ultrasonically cleaned with ethanol and thoroughly dried. Care was taken to ensure the time between polishing of the specimen surface and immersion of the sample to begin corrosion testing was minimal to reduce exposure to the atmosphere and subsequent formation of an oxide layer. A standard three electrode cell (PARSTAT 2263, Princeton Applied Research, USA) was employed with a saturated calomel electrode, platinum counter-electrode and the specimen as the working electrode. All test were performed at 37 ± 1 °C in Hank's balanced salt solution (H1387, Sigma-Aldrich, USA) (pH 7.2-7.4) with added 0.353 g/L of sodium bicarbonate. Solution was freshly prepared half an hour before each test (to allow the solution to reach 37 °C) in order to minimise degradation of the solution. A minimum of three tests were performed per manufacturing method. Open circuit potential (OCP) was measured for 150 minutes to allow for surface stabilisation in the Hank's balanced salt solution. Electrochemical impedance spectroscopy (EIS) was performed at OCP using a single sine acquisition mode with an applied amplitude of 10mV with scanning frequency ranging between 100 kHz and 10 mHz. Subsequently linear polarisation testing was carried out from ± 0.25 V (vs. SCE) at a scan rate of 0.166 mV/s. All electrochemical tests were performed in duplicates with two tests per duplicate.

The corrosion rate was calculated based on ASTM G59-97 using:

$$CR = 3.27 \times 10^{-3} \frac{i_{corr} EW}{\rho} \quad (1)$$

Where CR is the corrosion rate, i_{corr} is the corrosion current density, EW is the equivalent weight and ρ is the theoretical density of pure Fe, and kept constant regardless of the manufacturing method. The reaction $Fe \rightarrow Fe^{2+}$ was used to calculate EW.

2.5 Statistical analysis

Analysis of variance (ANOVA) was employed to assess the statistical significance of the process on mechanical properties and corrosion behaviour. Elastic modulus, yield stress, and compression stress were assessed in terms of mechanical properties. The current density was evaluated in terms of corrosion behaviour since it is directly related to the corrosion rate. The statistical significance level was fixed at 0.05. Tukey pairwise comparisons were made with 95% confidence levels. Residuals were checked for normality, homogeneity and equality of variance. Minitab 18 was used for the calculations (Minitab Inc, State College, PA, USA).

3.0 Results and Discussion

3.1 Material Characterization

XRD analysis was performed on the SLM-manufactured sample as it is the least equilibrium process, as such it has been chosen as a representative analysis. As can be seen in Figure 2 only the α-Fe phase is present. The other small peaks present correspond to surface Iron(III) oxide which formed due to minor atmospheric exposure.

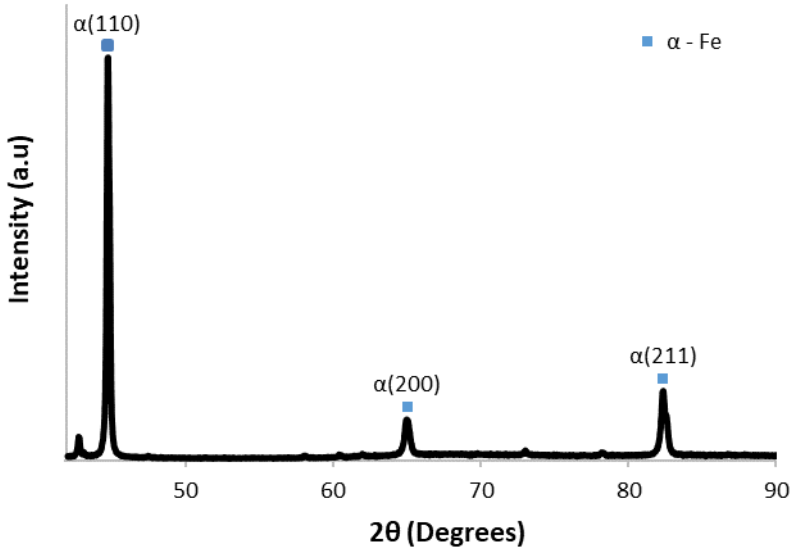

Figure 2 X-ray diffraction spectra of SLM-manufactured pure Fe

The microstructure of the pure Fe consists of α-ferrite, as seen in Figure 2, with the main effect of the different manufacturing methods on the microstructure being grain size and morphology (grain size quantified in Figure 4).

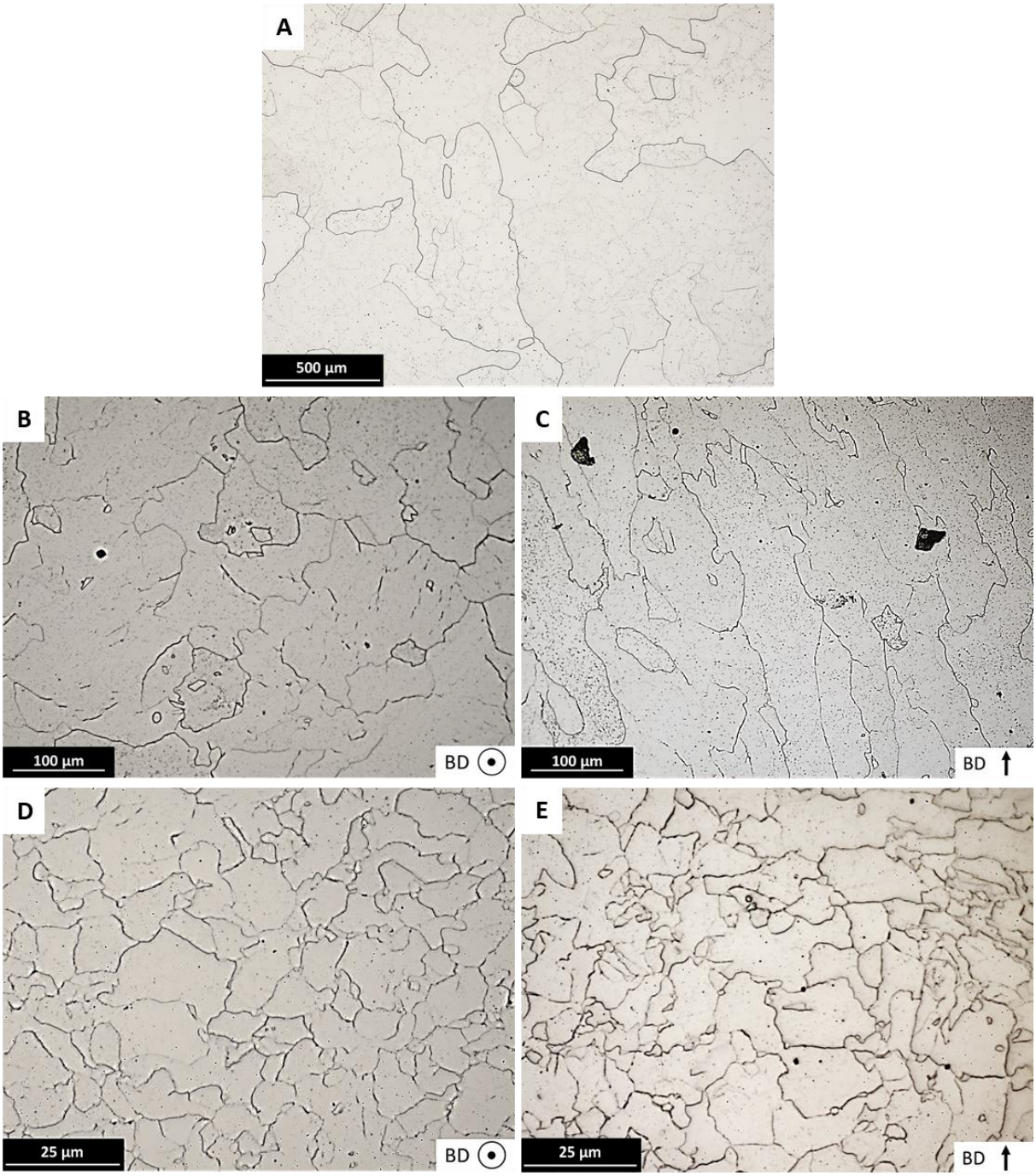

Figure 3 Optical Micrograph of pure Fe showing the microstructure of cast (A), LMD (B) with build direction (BD) out of plane, (C) LMD with build direction in plane, (D) SLM with build direction out of plane and (E) SLM with build direction in plane and E). Please note difference in magnification to better show the different microstructures.

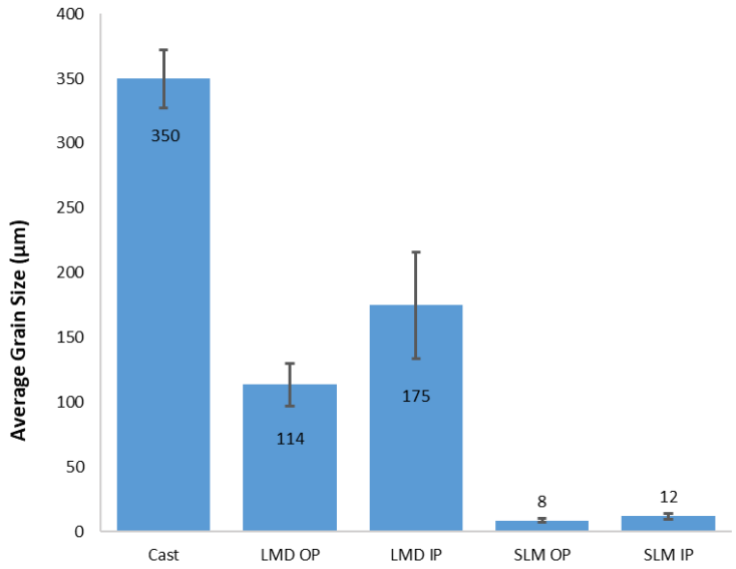

Figure 4 Average grain size of each manufacturing method. Error bars represent SD. IP denotes build direction in plane, OP denotes build direction out of plane.

The cast microstructure consists of coarse equiaxed α-ferrite, which is expected from a slow cooling rate. The typical cooling rate of castings is between $10^1 – 10^2$ K/s [33], with the centre of having the slowest cooling rate. For this study samples were machined from the centre of a relatively large casting, which was poured into a preheated mould and air cooled, likely resulting in cooling rates on the lower end of the range mentioned above.

Laser based additive manufacturing (AM) methods typically have small melt pools and high cooling rates [34], so it is expected that the grain size will be finer. From Figure 3 and Figure 4 it is clear that this is certainly the case, however, there is also a significant difference between the grain size of LMD and SLM manufactured samples. For this study the energy density used to manufacture the LMD samples was 113 J/mm^3 compared to 67 J/mm^3 used during SLM. Generally a higher energy density will increase the thermal accumulation in the melt pool subsequently decreasing the cooling rate. Furthermore, the scan speed and beam sizes also differ greatly between the processes. This can be seen by the difference in the typical cooling rates during LMD ($10^2 – 10^3$ K/s [35]) and SLM ($10^3 – 10^8$ K/s [36]). As the solidification rate is proportional to the cooling rate, the higher solidification rate that occurs during SLM will suppress grain growth resulting in finer grains [37]. Furthermore, the larger thermal accumulation present during LMD increases the amount of re-melting and duration of reheating of previous layers [35].

SLM typically results in microstructures with columnar grains growing preferentially in the build direction [38]. This tendency to form columnar grains occurs due to a combination of the thermal environment within the molten pool (i.e. steep temperature gradient which makes nucleation of equiaxed grains difficult), as well as the requirement for nucleant particles (substrates for heterogeneous nucleation) and alloy solute to generate constitutional supercooling [39]. For pure Fe manufactured via SLM however, the microstructure consists of predominately equiaxed grains with few elongated columnar grains [22, 40]. While this may appear at odds to what we know of the solidification process during SLM, especially given that this is pure Fe with no solute to provide constitutional supercooling, it is important to remember that the α-ferrite grains seen in the microstructure are far removed from the initial solidified structure (L → δ → γ → α). As in other alloy systems, solidification of the δ-phase most likely formed epitaxially grown columnar grains, but in this case the series of subsequent solid state transformations has produced a final room temperature microstructure with mostly equiaxed α ferrite grains (Figure 3). However, like other polymorphic metals, usually some orientation relationship exists with the parent grain which may explain why some slightly elongated α-ferrite grains align with the BD. For the Fe produced by LMD (Figure 3-C), the larger grain size shows this residual texture more clearly.

3.2 Mechanical Properties

ANOVA results showed that the manufacturing process did not provide a change on the Young's modulus, as shown in Table 3, with a p-value of 0.828. This is expected because the Young's modulus is an intrinsic material property [41]. The yield stress, however, is evidently affected by the manufacturing process as seen in Figure 5, with SLM having the highest yield stress, followed by LMD and then the cast sample. On the other hand, ANOVA results confirmed that the manufacturing process has a significant impact on both the yield stress and compressive strength with a p-value of 0.000. Tukey pairwise comparisons also showed that all processes were different for both the responses.

Song et al. proposed that the overall strength of α-Fe can be contributed to [22]:

$$\sigma = \Delta\sigma_{gr} + \Delta\sigma_{wh} + \Delta\sigma_{ps} \quad (2)$$

Where $\Delta\sigma_{gr}$ is the yield strength due to grain refinement, $\Delta\sigma_{wh}$ is the yield strength due to work hardening and $\Delta\sigma_{ps}$ is the yield strength due to secondary phase precipitation. The Hall – Petch relation states that the yield strength contribution of grain refinement is inverse to the grain size [41]. Finer microstructure restricts dislocation motion due to the higher number of grain boundaries present. The contribution to the overall strength by work hardening is proportional to the dislocation density [22, 42]. During compression testing the dislocation density is increased, which in turn results in higher strain fields on the lattice. This increases the amount of energy required for dislocation motion, and thus increasing the overall strength [41]. Furthermore, the dislocation density, and thus strength by work hardening, is further increased by the high cooling rates that occur during SLM [43]. Pure Fe manufactured by SLM has been found to contain small amounts of spherical secondary phase precipitates [22]. The load bearing-effect caused by these particles prevents dislocation motion, and thus the strengthening mechanism due to secondary phase precipitation is proportional to the volume fraction of particles [44]. Using Eq 2. Song et al. found that for α-ferrite the contribution to the overall strength by grain refinement was approximately 87.5%, significantly higher than that of work hardening (≈12.25%), with secondary phase precipitation having a negligible impact on the overall strength (≈0.25%). Both of the major strengthening mechanisms present are proportional to the cooling rate [22, 43], which explains why the SLM-manufactured pure Fe has the highest yield and compressive strength compared to its cast and LMD equivalents.

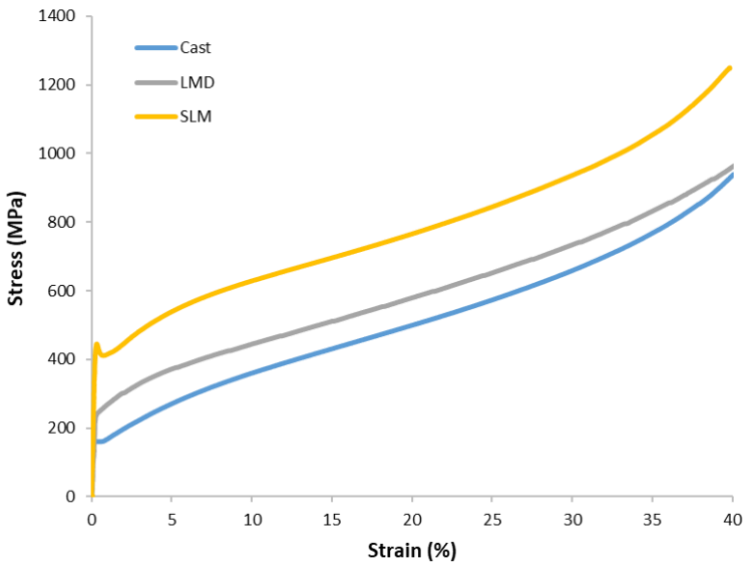

Figure 5 Compression curves for each manufacturing method

Table 3 Young's modulus, 0.2% offset yield point and compressive strength at 20% strain of each manufacturing method.

	Young's Modulus (GPa)	0.2% Offset Yield Point (MPa)	Compressive Strength at 20% Strain (MPa)
Cast	202.5 ± 6.7	157.1 ± 7.7	497.8 ± 7.5
LMD	202.5 ± 5.3	241.9 ± 19	580.6 ± 4.2
SLM	199.7 ± 6.7	421.1 ± 16	760.2 ± 6.5

The yield point phenomenon can be observed in Figure 5 by an upper and lower yield point. For pure Fe this phenomenon is attributed to the Cottrel atmospheres that form due to segregation of interstitial impurities such as carbon [45]. The strain field induced by the Cottrel atmospheres pin dislocation movement requiring additional energy resulting in the upper yield point. Once enough energy has been provided the overcome the Cottrel atmospheres the energy required for dislocation movement is lower accounting for the lower yield point. Since there is a negligible amount of carbon atoms in the materials tested new Cottrel atmospheres cannot form at the new dislocation sites. This is contrary to high carbon steels wherein there is sufficient carbon to form Cottrell atmospheres throughout deformation resulting in a singular yield point.

Higher yield and ductility are desired for biomedical implants because as the implant degrades the mechanical properties do too [1]. During the degradation it is critical that the implant can still serve its function and provide support to the healing tissue. This is especially important for porous medical implants such as bone scaffolds as the high porosity levels of these implants can significantly reduce the strength which in turn is further affected by the higher degradation rates of scaffolds. When used for bone implants the high Young's modulus of bulk pure Fe (approx. 200 GPa) can lead to stress shielding resulting in bone resorption [46]. However, using SLM, hierarchal porous Fe implants had a stiffness two orders of magnitude lower than that of bulk Fe [19]. As such, SLM is an ideal candidate for these bone scaffolds as it can achieve complex geometries with minimal post-processing and has improved mechanical properties when compared to LMD or cast equivalents.

3.2 Corrosion

The more negatively shifted corrosion potential of the SLM, as seen in Figure 6-A, shows that SLM has a higher tendency for corrosion. ANOVA results showed that the manufacturing process had an effect on corrosion current, hence corrosion rate had a p-value at 0.000 for both cases. Tukey pairwise comparisons also showed that all processes were different for both the responses. This can

be further seen in Table 4, which shows that corrosion rate of pure Fe manufactured via SLM is over fifty percent higher compared to the cast sample. One reason for this could be due the difference in grain size resultant from the different manufacturing methods as shown in Figure 4. The effect of grain size on corrosion rate is highly dependent on the metal and the environment it is exposed to. For pure Fe in physiological solution some studies suggest smaller grain size increases corrosion rates [19, 47], whereas other studies have shown it reduces the rate of corrosion [48, 49]. Ralston and Birbilis proposed a general relationship between the grain size and corrosion current [50]:

$$i_{corr} = A + Bd^{-\frac{1}{2}} \tag{3}$$

Where A and B are constants and d is the grain size. In a passive medium B is negative and thus the corrosion rate is proportional to the grain size. In this case a decrease in grain size stabilises the passive film reducing the corrosion rate. On the other hand, in an active medium B is positive and thus a decrease in grain size increases the corrosion rate. Under these circumstances a finer microstructure increases the volume of grain boundaries which in turns increases the reactivity of the material [51]. Another factor contributing to the difference in corrosion rates could be the higher presence of dislocations and impurities in the AM samples, which can increase the corrosion rates [52, 53].

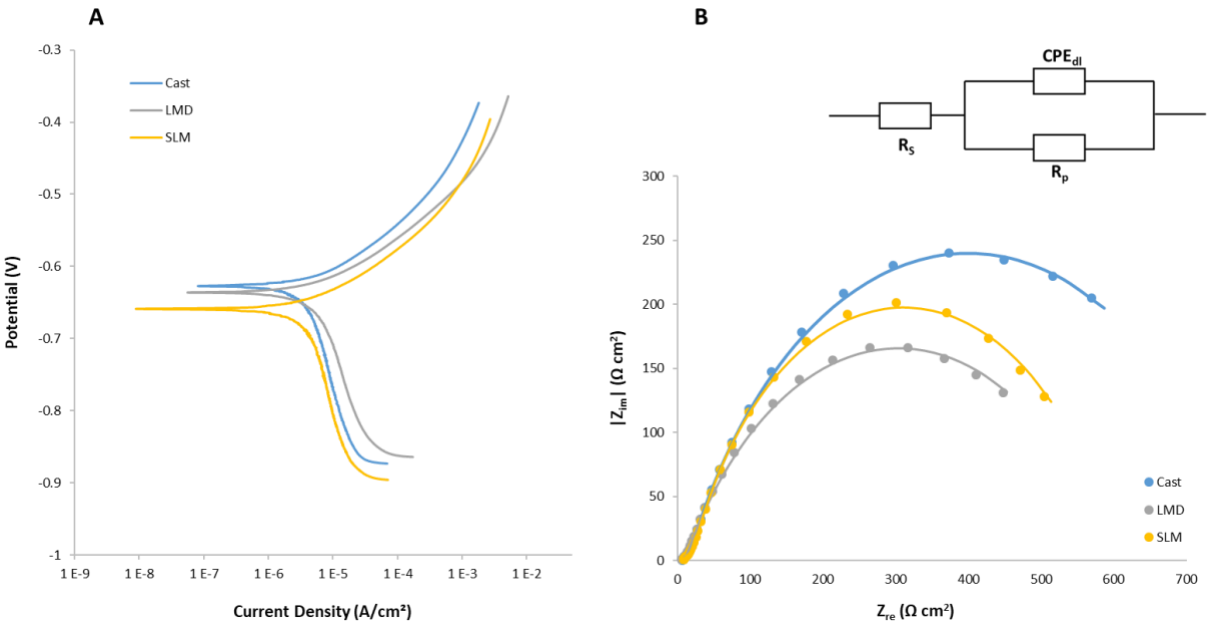

Figure 6 Polarization curves (A) and Nyquist plots with proposed equivalent circuit model to fit the EIS data (B), for each manufacturing method.

Table 4 Electrochemical data and Corrosion rate of each manufacturing method.

	i_{corr} (µA/cm^2)	CR (µm/yr)	R_S (Ω cm^2)	Q_{dl} (mS.s^n/cm^2)	n_{dl}	R_p (Ω cm^2)
Cast	4.05 ± 0.3	47 ± 3	25	0.45	0.72	1410
LMD	5.72 ± 0.1	66 ± 1	25	0.64	0.66	1030
SLM	6.2 ± 0.1	72 ± 1	25	0.37	0.75	1035

The Nyquist plots shown in Figure 6-B are not perfectly semicircular, likely due to frequency dispersion [54]. EIS data was fitted with an equivalent circuit (inset Figure 6-B) and results tabulated in Table 4. The low frequency range was ignored in the model fitting as lower frequency measurements can be disturbed by the concurrent degradation [55]. In the equivalent model proposed, R_S represents the resistance of the electrolyte, CPE_{dl} represents the double layer capacitance and R_p the polarization resistance. A constant phase element (CPE) was used to represent the non-ideal dielectric behaviour of the working electrode due to the possible presence of non-homogenous surface coating, impurities, dislocations and grain boundaries and is represented by Q_{dl} (the CPE value) and n_{dl} (the CPE exponent). In the present case as n_{dl} varies between 0.65-0.8 the CPE defines a dielectric relaxation time in frequency space [56].

In general, higher values of R_p represents a lower dissolution rate of the exposed metal [57], which is in line with the cast results, as it has the highest polarization resistance and lowest corrosion rate. Interestingly, the R_p of the LMD and SLM manufactured samples are comparable, but the CR of the SLM sample is slightly higher. Given that i_{corr}, and thus the corrosion rate, is related to both R_p and CPE_{dl}, the higher CR of SLM manufactured samples can be attributed to the difference in Q_{dl}. The term Q_{dl} is associated with the area on the working electrode surface where cathodic reactions are possible [58]. The smaller Q_{dl} of the SLM samples results in localised corrosion due to smaller cathodic sites and so attributes for the difference in corrosion rate. The localised corrosion experienced by the SLM is not in agreement with previous research, which showed that for pure Fe in an active passive medium such as Hank's solution, a reduction in grain size encourages a higher rate of uniform corrosion and reduces the amount of localised corrosion [53, 59]. This difference in results is possibly due the high internal defect, dislocation and residual stress density that is imparted due to the high cooling rates of SLM [22, 23], which can locally destabilise the passive film [60]. Local film destabilisation in SLM samples could be reduced by decreasing the internal defect, dislocation and residual stress density by lowering the cooling rate during SLM or by subsequent

heat treatment. However, this could have consequences on the corrosion rate as the former results in grain coarsening while previous studies have shown that the latter results in recrystallization of finer grains driven by the high residual stresses present in SLM pure Fe [23].

Localised corrosion is not desired for small, thin implants such as stents where it can cause premature failure of the implant. However, for scaffolds, the failure of local struts should not significantly affect the bulk mechanical properties during corrosion, but will increase the overall degradation rate [19]. Furthermore, the ingrowth of bone into the scaffold results in stress transferring from the scaffold to the bone throughout healing, reducing the effect of localised corrosion on the mechanical properties of the scaffold. For biodegradable pure Fe a higher corrosion rate is preferable as the corrosion rate is often deemed too slow [14]. This slow corrosion rate causes the implant to behave like a permanent metal in the body which can invoke foreign body reactions that can cause implant loosening and subsequent rejection [1]. As such, the ability of SLM to manufacture complex geometries, improve mechanical properties and increase corrosion rates when compared to its cast counterpart lends this technology to the manufacturing of biodegradable iron implants.

Conclusion

In this study the microstructural, corrosion and mechanical properties of cast, LMD and SLM manufactured pure Fe for biodegradable biomedical implant applications were investigated. The cast pure Fe had an average grain size over 30 times that of SLM and double that of LMD due to the significantly higher cooling rates of the laser based AM processes, which lead to higher mechanical properties of the SLM processed pure Fe. Furthermore, the corrosion rates of pure Fe manufactured via LMD and SLM were approximately fifty percent higher than its cast equivalent. Hence, as SLM can produce higher precision and better process resolution parts than LMD, its capacity to produce custom implants, with increased corrosion rates and improved mechanical properties when compared to its cast counterpart lends this technology to the manufacturing of biodegradable iron implants.

Acknowledgements

DC, MJB, DK and MSD acknowledge the support of the School of Mechanical and Mining Engineering, the Queensland Centre for Advanced Materials processing and Manufacturing and the Australian Research Council Research Hub for Advanced Manufacturing of Medical Devices (IH150100024). AGD, and BP acknowledge the support of European Union, Repubblica Italiana, Regione Lombardia and FESR for the project MADE4LO under the call "POR FESR 2014-2020 ASSE I - AZIONE I.1.B.1.3". MJB also acknowledges the support of the Australian Research Council Discovery Program and is in receipt of Discover Early Career Researcher Award (DE160100260).

References

[1] Y.F. Zheng, X.N. Gu, F. Witte, Biodegradable metals, Materials Science and Engineering: R: Reports 77 (2014) 1-34.
[2] M. Navarro, A. Michiardi, O. Castaño, J.A. Planell, Biomaterials in orthopaedics, Journal of the Royal Society Interface 5(27) (2008) 1137-1158.
[3] Y. Okazaki, E. Gotoh, Comparison of metal release from various metallic biomaterials in vitro, Biomaterials 26(1) (2005) 11-21.
[4] H. Li, Y. Zheng, L. Qin, Progress of biodegradable metals, Progress in Natural Science: Materials International 24(5) (2014) 414-422.
[5] F. Witte, Reprint of: The history of biodegradable magnesium implants: A review, Acta Biomaterialia 23 (2015) S28-S40.
[6] J. Vormann, Magnesium: nutrition and metabolism, Molecular Aspects of Medicine 24(1) (2003) 27-37.
[7] M.G. Seelig, A study of magnesium wire as an absorbable suture and ligature material, Archives of Surgery 8(2) (1924) 669-680.
[8] M.P. Staiger, A.M. Pietak, J. Huadmai, G. Dias, Magnesium and its alloys as orthopedic biomaterials: A review, Biomaterials 27(9) (2006) 1728-1734.
[9] P.K. Bowen, J. Drelich, J. Goldman, Zinc Exhibits Ideal Physiological Corrosion Behavior for Bioabsorbable Stents, Advanced Materials 25(18) (2013) 2577-2582.
[10] E. Mostaed, M. Sikora-Jasinska, A. Mostaed, S. Loffredo, A.G. Demir, B. Previtali, D. Mantovani, R. Beanland, M. Vedani, Novel Zn-based alloys for biodegradable stent applications: Design, development and in vitro degradation, Journal of the Mechanical Behavior of Biomedical Materials 60 (2016) 581-602.
[11] P.K. Bowen, E.R. Shearier, S. Zhao, R.J. Guillory, F. Zhao, J. Goldman, J.W. Drelich, Biodegradable Metals for Cardiovascular Stents: from Clinical Concerns to Recent Zn-Alloys, Advanced Healthcare Materials 5(10) (2016) 1121-1140.

[12] H.K. Lim, J.L. Riddell, A.C. Nowson, O.A. Booth, A.E. Szymlek-Gay, Iron and Zinc Nutrition in the Economically-Developed World: A Review, Nutrients 5(8) (2013).
[13] D.T. Chou, D. Wells, D. Hong, B. Lee, H. Kuhn, P.N. Kumta, Novel processing of iron–manganese alloy-based biomaterials by inkjet 3-D printing, Acta Biomaterialia 9(10) (2013) 8593-8603.
[14] M. Peuster, C. Hesse, T. Schloo, C. Fink, P. Beerbaum, C. von Schnakenburg, Long-term biocompatibility of a corrodible peripheral iron stent in the porcine descending aorta, Biomaterials 27(28) (2006) 4955-4962.
[15] H. Hermawan, D. Dubé, D. Mantovani, Degradable metallic biomaterials: Design and development of Fe–Mn alloys for stents, Journal of Biomedical Materials Research Part A 93A(1) (2010) 1-11.
[16] J. He, F.-L. He, D.-W. Li, Y.-L. Liu, Y.-Y. Liu, Y.-J. Ye, D.-C. Yin, Advances in Fe-based biodegradable metallic materials, RSC Advances 6(114) (2016) 112819-112838.
[17] M. Peuster, P. Wohlsein, M. Brügmann, M. Ehlerding, K. Seidler, C. Fink, H. Brauer, A. Fischer, G. Hausdorf, A novel approach to temporary stenting: degradable cardiovascular stents produced from corrodible metal—results 6–18 months after implantation into New Zealand white rabbits, Heart 86(5) (2001) 563.
[18] B.V. Krishna, S. Bose, A. Bandyopadhyay, Low stiffness porous Ti structures for load-bearing implants, Acta Biomaterialia 3(6) (2007) 997-1006.
[19] Y. Li, H. Jahr, K. Lietaert, P. Pavanram, A. Yilmaz, L.I. Fockaert, M.A. Leeflang, B. Pouran, Y. Gonzalez-Garcia, H. Weinans, J.M.C. Mol, J. Zhou, A.A. Zadpoor, Additively manufactured biodegradable porous iron, Acta Biomaterialia 77 (2018) 380-393.
[20] H. Fayazfar, M. Salarian, A. Rogalsky, D. Sarker, P. Russo, V. Paserin, E. Toyserkani, A critical review of powder-based additive manufacturing of ferrous alloys: Process parameters, microstructure and mechanical properties, Materials & Design 144 (2018) 98-128.
[21] M. Montani, A.G. Demir, E. Mostaed, M. Vedani, B. Previtali, Processability of pure Zn and pure Fe by SLM for biodegradable metallic implant manufacturing, Rapid Prototyping Journal 23(3) (2017) 514-523.
[22] B. Song, S. Dong, S. Deng, H. Liao, C. Coddet, Microstructure and tensile properties of iron parts fabricated by selective laser melting, Optics & Laser Technology 56 (2014) 451-460.
[23] B. Song, S. Dong, Q. Liu, H. Liao, C. Coddet, Vacuum heat treatment of iron parts produced by selective laser melting: Microstructure, residual stress and tensile behavior, Materials & Design (1980-2015) 54 (2014) 727-733.
[24] J. Čapek, D. Vojtěch, A. Oborná, Microstructural and mechanical properties of biodegradable iron foam prepared by powder metallurgy, Materials & Design 83 (2015) 468-482.
[25] H. Hermawan, D. Dubé, D. Mantovani, Degradable metallic biomaterials: Design and development of Fe–Mn alloys for stents, Journal of Biomedical Materials Research Part A 93A(1) (2009) 1-11.
[26] B. Liu, Y.F. Zheng, Effects of alloying elements (Mn, Co, Al, W, Sn, B, C and S) on biodegradability and in vitro biocompatibility of pure iron, Acta Biomaterialia 7(3) (2011) 1407-1420.
[27] R. Tolouei, J. Harrison, C. Paternoster, S. Turgeon, P. Chevallier, D. Mantovani, The use of multiple pseudo-physiological solutions to simulate the degradation behavior of pure iron as a metallic resorbable implant: a surface-characterization study, Physical Chemistry Chemical Physics 18(29) (2016) 19637-19646.
[28] B.S. Institution, ISO 3369: Impermeable sintered metal materials and hardmetals. Determination of density, 2010.
[29] ASTM International, Standard Test Methods for Determining Average Grain Size, ASTM International,, PA, United States, 2014.
[30] A.S.f.T.a. Materials, ASTM E9 - 09: Standard Test Methods of Compression Testing of Metallic Materials at Room Temperature, 2018.
[31] A.S.f.T.a. Materials, ASTM F3122 - 14: Standard Guide for Evaluating Mechanical Properties of Metal Materials Made via Additive Manufacturing Processes.

[32] A.S.f.T.a. Materials, ASTM G59 - 97: Standard Test Method for Conducting Potentiodynamic Polarization Resistance Measurements, 2014.
[33] J.-C. Zhao, M.R. Notis, Continuous cooling transformation kinetics versus isothermal transformation kinetics of steels: a phenomenological rationalization of experimental observations, Materials Science and Engineering: R: Reports 15(4) (1995) 135-207.
[34] L.-E. Loh, C.-K. Chua, W.-Y. Yeong, J. Song, M. Mapar, S.-L. Sing, Z.-H. Liu, D.-Q. Zhang, Numerical investigation and an effective modelling on the Selective Laser Melting (SLM) process with aluminium alloy 6061, International Journal of Heat and Mass Transfer 80 (2015) 288-300.
[35] W. Hofmeister, M. Griffith, Solidification in direct metal deposition by LENS processing, JOM 53(9) (2001) 30-34.
[36] D. Buchbinder, H. Schleifenbaum, S. Heidrich, W. Meiners, J. Bültmann, High Power Selective Laser Melting (HP SLM) of Aluminum Parts, Physics Procedia 12 (2011) 271-278.
[37] H. Attar, S. Ehtemam-Haghighi, D. Kent, X. Wu, M.S. Dargusch, Comparative study of commercially pure titanium produced by laser engineered net shaping, selective laser melting and casting processes, Materials Science and Engineering: A 705 (2017) 385-393.
[38] L. Thijs, F. Verhaeghe, T. Craeghs, J.V. Humbeeck, J.-P. Kruth, A study of the microstructural evolution during selective laser melting of Ti–6Al–4V, Acta Materialia 58(9) (2010) 3303-3312.
[39] M.J. Bermingham, D.H. StJohn, J. Krynen, S. Tedman-Jones, M.S. Dargusch, Promoting the columnar to equiaxed transition and grain refinement of titanium alloys during additive manufacturing, Acta Materialia (2019).
[40] D. Carluccio, A.G. Demir, L. Caprio, B. Previtali, M. Bermingham, M. Dargusch, The Influence of Processing Parameters on Pure Fe and Fe-35Mn Scaffolds Produced by Selective Laser Melting, Journal of Manufacturing Processes, Submitted (2019).
[41] W.D. Callister, D.G. Rethwisch, Materials science and engineering, Ninth edition, SI version.. ed., Singapore : John Wiley & Sons Asia Pte Ltd2015.
[42] M.E. Kassner, Taylor hardening in five-power-law creep of metals and Class M alloys, Acta Materialia 52(1) (2004) 1-9.
[43] L.E. Murr, S.A. Quinones, S.M. Gaytan, M.I. Lopez, A. Rodela, E.Y. Martinez, D.H. Hernandez, E. Martinez, F. Medina, R.B. Wicker, Microstructure and mechanical behavior of Ti–6Al–4V produced by rapid-layer manufacturing, for biomedical applications, Journal of the Mechanical Behavior of Biomedical Materials 2(1) (2009) 20-32.
[44] S. Scudino, G. Liu, M. Sakaliyska, K.B. Surreddi, J. Eckert, Powder metallurgy of Al-based metal matrix composites reinforced with β-Al3Mg2 intermetallic particles: Analysis and modeling of mechanical properties, Acta Materialia 57(15) (2009) 4529-4538.
[45] E.O. Hall, Iron and its Alloys, in: E.O. Hall (Ed.), Yield Point Phenomena in Metals and Alloys, Springer US, Boston, MA, 1970, pp. 65-126.
[46] D.M. Robertson, L. Pierre, R. Chahal, Preliminary observations of bone ingrowth into porous materials, Journal of biomedical materials research 10(3) (1976) 335-44.
[47] M. Moravej, F. Prima, M. Fiset, D. Mantovani, Electroformed iron as new biomaterial for degradable stents: Development process and structure–properties relationship, Acta Biomaterialia 6(5) (2010) 1726-1735.
[48] C.S. Obayi, R. Tolouei, A. Mostavan, C. Paternoster, S. Turgeon, B.A. Okorie, D.O. Obikwelu, D. Mantovani, Effect of grain sizes on mechanical properties and biodegradation behavior of pure iron for cardiovascular stent application, Biomatter 6(1) (2016) e959874.
[49] T. Jurgeleit, E. Quandt, C. Zamponi, Magnetron Sputtering a New Fabrication Method of Iron Based Biodegradable Implant Materials, Advances in Materials Science and Engineering 2015 (2015) 9.
[50] K.D. Ralston, N. Birbilis, C.H.J. Davies, Revealing the relationship between grain size and corrosion rate of metals, Scripta Materialia 63(12) (2010) 1201-1204.
[51] K.D. Ralston, N. Birbilis, Effect of Grain Size on Corrosion: A Review, CORROSION 66(7) (2010) 075005-075005-13.

[52] S. Yin, D.Y. Li, Effects of prior cold work on corrosion and corrosive wear of copper in HNO3 and NaCl solutions, Materials Science and Engineering: A 394(1) (2005) 266-276.
[53] C.S. Obayi, R. Tolouei, C. Paternoster, S. Turgeon, B.A. Okorie, D.O. Obikwelu, G. Cassar, J. Buhagiar, D. Mantovani, Influence of cross-rolling on the micro-texture and biodegradation of pure iron as biodegradable material for medical implants, Acta Biomaterialia 17 (2015) 68-77.
[54] K. Jüttner, Electrochemical impedance spectroscopy (EIS) of corrosion processes on inhomogeneous surfaces, Electrochimica Acta 35(10) (1990) 1501-1508.
[55] N.T. Kirkland, N. Birbilis, M.P. Staiger, Assessing the corrosion of biodegradable magnesium implants: A critical review of current methodologies and their limitations, Acta Biomaterialia 8(3) (2012) 925-936.
[56] E.M.A. Martini, I.L. Muller, Characterization of the film formed on iron in borate solution by electrochemical impedance spectroscopy, Corrosion Science 42(3) (2000) 443-454.
[57] B.R. Hinderliter, S.G. Croll, D.E. Tallman, Q. Su, G.P. Bierwagen, Interpretation of EIS data from accelerated exposure of coated metals based on modeling of coating physical properties, Electrochimica Acta 51(21) (2006) 4505-4515.
[58] Y. Liu, M. Curioni, Z. Liu, Correlation between electrochemical impedance measurements and corrosion rates of Mg-1Ca alloy in simulated body fluid, Electrochimica Acta 264 (2018) 101-108.
[59] S. Zhu, N. Huang, L. Xu, Y. Zhang, H. Liu, H. Sun, Y. Leng, Biocompatibility of pure iron: In vitro assessment of degradation kinetics and cytotoxicity on endothelial cells, Materials Science and Engineering: C 29(5) (2009) 1589-1592.
[60] T. Yamamoto, K. Fushimi, S. Miura, H. Konno, Influence of substrate dislocation on passivation of pure iron in pH 8.4 borate buffer solution, Journal of The Electrochemical Society 157(7) (2010) C231-C237.